Elucidating Electrocatalytic Oxygen Reduction Kinetics via Intermediates by Time-Dependent Electrochemiluminescence

Kaiqing Wu, Ran Chen, Zhixin Zhou, Xinghua Chen, Yanqin Lv, Jin Ma, Yanfei Shen, Songqin Liu, Yuanjian Zhang*
Jiangsu Engineering Laboratory of Smart Carbon-Rich Materials and Device, Jiangsu Province Hi-Tech Key Laboratory for Bio-Medical Research, State Key Laboratory of Bioelectronics, School of Chemistry and Chemical Engineering, Medical School, Southeast University, Nanjing 21189, China. Email: Yuanjian.Zhang@seu.edu.cn

Abstract

Facile evaluation of oxygen reduction reaction (ORR) kinetics for massive electrocatalysts is critical for sustainable fuel cells development and industrial H_2O_2 production. Despite great success in ORR studies by mainstream strategies, such as membrane electrode assembly, rotation electrode technique and advanced surface-sensitive spectroscopy, the time/spatial distribution of reactive oxygen species (ROS) intermediates in the diffusion layer is still unknown. By time-dependent electrochemiluminescence (Td-ECL), here we report an intermediate-oriented methodology for ORR kinetics analysis. Thanks to multiple ultra-sensitive stoichiometric reactions between ROS and the ECL emitter, except for electron transfer numbers and rate constants, the potential-dependent time/spatial distribution of ROS was successfully obtained for the first time. Such uncovered exclusive information would guide fuel cells and H_2O_2 production with maximized activity and durability, for instance, a larger overpotential would be beneficial to electrocatalysts of $2e^-$ reduction for H_2O_2 production, because of the high yield of H_2O_2 and low concentration of attackable $O_2^{\bullet-}$. This work would pave the exploration of not only the fundamentals of unambiguous ORR mechanism but also the durability of electrocatalysts for practical applications.

Keywords: Oxygen reduction reaction, Kinetics, Electrocatalysts, Reactive oxygen species, Time-dependent electrochemiluminescence

Introduction

Carbon neutrality is widely regarded as the ultimate way to address global warming and achieve a sustainable world. Among them, fuel cells have garnered increasing attention as a promising solution since it does not emit carbon dioxide during the conversion of chemical energy into electricity, and the theoretical efficiency is near-unity.[1] However, owing to multiple electron-transfer processes, the oxygen reduction reaction (ORR), the cathodic reaction in fuel cells, is kinetically sluggish, which significantly hampered the commercialization of fuel cells.[2] Along this line, developing ORR electrocatalysts with high activity, reasonable durability, and low cost has been intensively explored for several decades,[3] in which accurate and fast screening ORR kinetics is essential to examine electrocatalyst and give feedback in preparation.

The membrane electrode assembly (MEA), primarily consisting of the proton exchange membrane, catalyst layer, and gas diffusion layer, is the closest to the actual fuel cell use and adept at giving the ultimate performance of electrocatalysts.[1b, 4] Nevertheless, its operation is time-consuming and need costly equipment, professional expertise, and a large number of samples.[5] In this event, newly developed electrocatalysts, often in small amounts, are preferred to be examined by laboratory testing from a fundamental point of view before applying in MEA or realistic fuel cells. For this reason, the rotation electrode technique, including rotating disk electrode (RDE) and rotating ring disk electrode (RRDE), has been the most common way to obtain the intrinsic activities of ORR electrocatalysts.[6] The Koutecky-Levich (K-L) equation describes the current density of electrocatalysts on RDE (Eq. S1-3). The selectivity of H_2O_2 and the associated electron transfer number (n) during ORR can also be calculated by RRDE (Eq. S4, 5). Nonetheless, due to the lack of consideration for intermediates, MEA and RDE/RRDE methods can hardly offer information of intermediate reactive oxygen species (ROS), such as $O_2^{\bullet-}$, which is critical to the fundamental exploration of unambiguous ORR mechanism[7] and the durability concern of electrocatalysts for practical applications.[8]

Indeed, ROS are produced at the surface of electrocatalysts, which have recently been confirmed by surface-sensitive spectroscopic methods, such as surface-enhanced

infrared reflection absorption spectroscopy (SEIRAS)[9] and surface-enhanced Raman scattering (SERS).[10] Moreover, the dissolved ROS were observed in ORR by scanning electrochemical microscopy (SECM), but the extremely short distance between ultramicroelectrode and substrate, typically tens of nanometers to several micrometers, requires smooth electrocatalyst, restricting its general applications.[11] Notably, although the generation of ROS on the surface of electrocatalysts and the existence of dissolved ROS have been observed, the quantitative time/spatial distribution of ROS intermediates is still unknow,[12] owing to challenges in facile quantitative detection of these trace and short-lived ROS.

Due to theoretical zero background and simple instrumentation, electrochemiluminescence or electrogenerated chemiluminescence (ECL), has drawn increasing attention across diverse fields, ranging from clinical diagnosis to super-resolved imaging.[13] As known, ROS are excellent co-reactants for luminol to gain a strong ECL signal.[14] For instance, the detection limit of H_2O_2 by ECL via $O_2^{\bullet-}$ pathway (Eq. 1-3) was three orders of magnitude superior to that by RRDE (Figure 1a), down to nM level. Thus, ROS-triggered ECL would be a powerful tool with a high signal-to-noise ratio to screen kinetics of ORR electrocatalysts. Nonetheless, although the highly sensitive ECL between luminol and ROS, including which produced in ORR,[15] has been established for several decades,[16] the quantitative ORR kinetics, particularly the time/spatial distribution of ROS intermediates in the vicinity of electrocatalysts, have been rarely reported using ECL.

Herein, we report a ROS-oriented strategy for kinetic evaluation of ORR electrocatalysts in alkaline media using time-dependent ECL (Td-ECL). The kinetic evaluation includes synchronous sequential ORR and ECL reactions driven by double-potential step chronoamperometry and the subsequent ECL intensity collection. Only commonly-used potentiostat, glassy carbon electrodes, and a photomultiplier (PMT) were required to drive ORR and detect trace-amount ROS intermediates in the diffusion layer. Interestingly, ORR electrocatalysts with two-/four-electron reduction could be reliably discriminated by ECL peak intensities using principal component analysis (PCA). Moreover, due to multiple ultrasensitive stoichiometric reactions between ROS

and the ECL luminophore, the quantitative kinetic information, such as apparent rate constant and potential-dependent time/spatial distribution of ROS were successfully extracted by finite element analysis (FEA) of the ECL decay curves.

Results and discussion

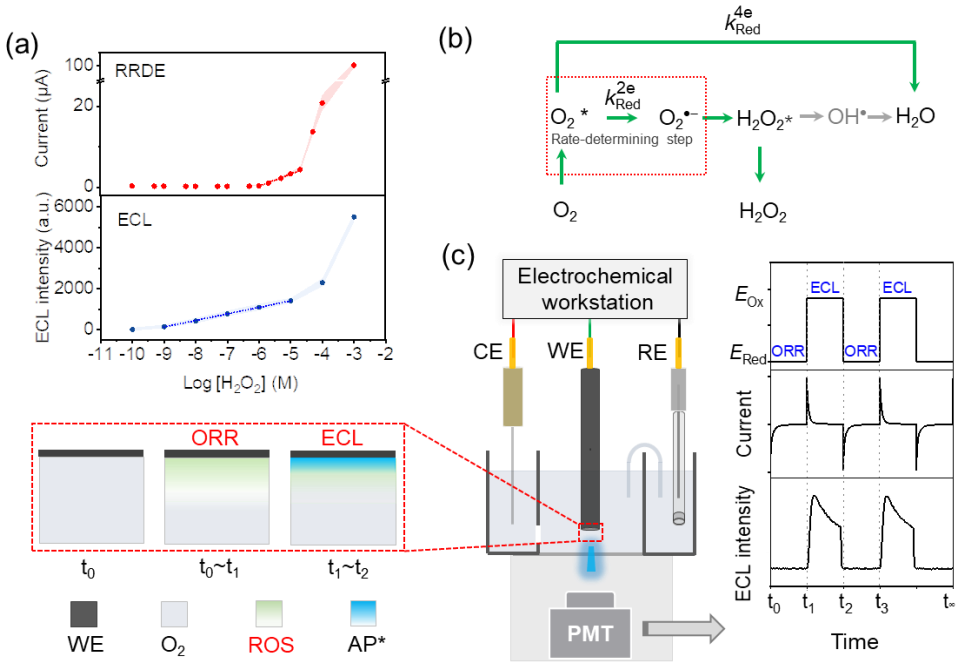

Figure 1. **Principle and setup of ECL for ORR kinetics evaluation.** (a) Responses of H_2O_2 at different concentrations by ECL and RRDE methods. The colored areas represent the standard error. (b) Reaction pathways of ORR in a modified Damjanovic model. (c) Brief setup of Td-ECL method for ORR kinetics analysis and the electrochemical/ECL signals at a different time during the Td-ECL measurement. The enlarged area and line charts show the dissolved O_2, ROS, and Ap* distribution in the diffusion layer.

The modified Damjanovic model for the ORR is shown in Figure 1b,[17] which generally consists of several parallel steps. For the typical four-electron ($4e^-$) transfer pathway, O_2 is directly reduced into H_2O by accepting four electrons. The sequential path involves a two-electron ($2e^-$) reduction of O_2 into H_2O_2 and a further reduction by another $2e^-$ reduction via $OH^\bullet$ as the intermediate into water. Alternatively, the reaction is stopped at the generation of H_2O_2 via $O_2^{\bullet-}$ as the intermediate, which is the representative $2e^-$ transfer pathway. For most electrocatalysts, $2e^-$ and $4e^-$ transfer pathways parallelly occur. Along the line, there were four preconditions for ECL to be applicable in ORR kinetics evaluation using the instruments in Figure 1c: (1) whether

ROS were generated in ORR; (2) would ROS trigger chemiluminescence of luminol; (3) could short-lived ROS produced during ORR be stable until the chemiluminescence was triggered; and (4) the side influence of exotic luminol on ORR is negligible or not.

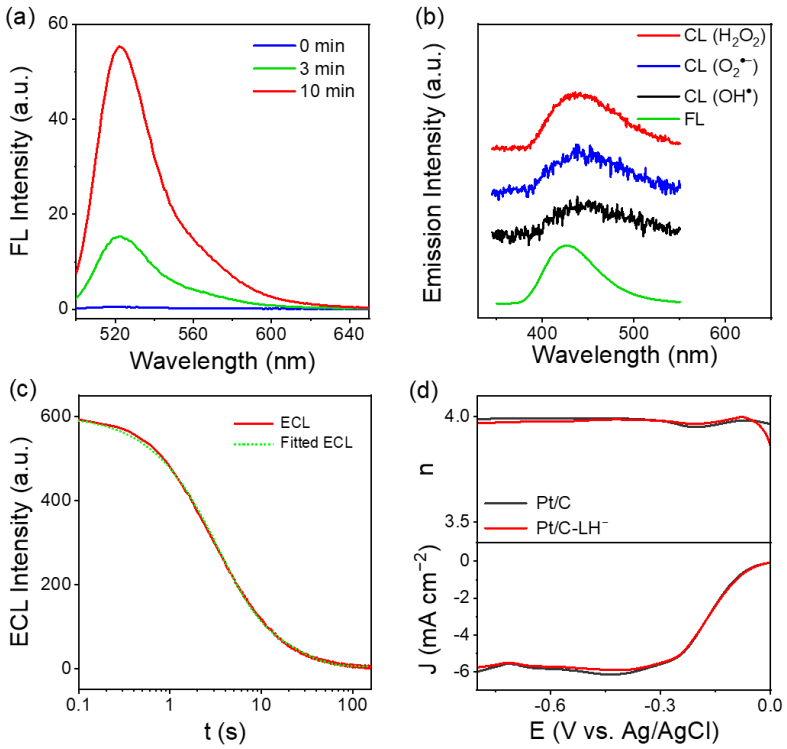

Figure 2. **Principle verification of ECL for ORR kinetics evaluation.** (a) Fluorescence spectra of DCDFH after reaction with ROS generated by ORR with different accumulated time. (b) Chemiluminescent spectra of luminol with H_2O_2 (red line), $O_2^{\bullet-}$ (blue line), $OH^{\bullet}$ (black line) collected by a minimized optic fiber grating spectrometer and FL spectrum of luminol (green line). (c) Intensity of ROS triggered ECL with time when ORR was off and the fitted curve. (d) Electron transfer number (n) and polarization curves for Pt/C by RRDE in O_2-saturated 0.1 M KOH with and without luminol (0.1 mM).

To validate these requirements, in the first set of experiments, 2,7-dichlorodihydrofluorescein diacetate (DCDFH) was used as an intermediate indicator, as it can chemically react with ROS, once which were formed, producing a fluorescent product.[18] Taking Zn-N-C ORR electrocatalyst as an example, it was observed that when a potential of –0.3 V was applied to drive ORR for a period of time, the typical fluorescence for the oxidized product of DCDFH was detected, and the fluorescent intensity accumulated upon the extended reaction time (Figure 2a, Figure S1). It verified the production of ROS in ORR that oxidized DCDFH. Complementarily, the trapping experiments for ROS were also explored. For this, dimethyl sulfoxide (DMSO)

and p-benzoquinone (BQ), which are the scavengers for $OH^{\bullet}$ and $O_2^{\bullet-}$, respectively, were selected to identify the types of ROS. Previous reports implied that the second-order rate constant of the reaction between DMSO and $OH^{\bullet}$ ($k = 5.4 \times 10^9$ M^{-1} s^{-1}) was greater than that of luminol with $OH^{\bullet}$ (4.8×10^9 M^{-1} s^{-1}).[19] However, the influence of DMSO on the ECL intensity was negligible, even when the concentration of DMSO was up to 10 mM (Figure S2a), suggesting $OH^{\bullet}$ was not apparently produced during ORR in alkaline conditions. Interestingly, BQ that has a reaction rate constant ($k = 9.6 \times 10^8$ M^{-1} s^{-1}) faster than luminol with $O_2^{\bullet-}$ ($k = 2.3 \times 10^8$ M^{-1} s^{-1}), demonstrated a clear inhibition of ECL under a low concentration of 0.2 mM (Figure S2b).[20] The decreased activity by raising the concentration of BQ in the reaction further demonstrated $O_2^{\bullet-}$ was generated during ORR in alkaline conditions, consistent with the modified Damjanovic model.

Next, we explored whether ROS could trigger the chemiluminescence of luminol. For this purpose, H_2O_2, $OH^{\bullet}$, and $O_2^{\bullet-}$, were individually produced by chemical reactions (Figure S3), and reacted with luminol. As shown in Figure 2b, the maximum emission at ca. 440 nm was observed in all cases, almost identical to the fluorescence spectrum of luminol. The noise and slight red shift of the chemiluminescence spectrum compared to the photoexcited spectrum was noticed, attributing to the lower S/N of minimized optic fiber grating spectrometer compared to the standard FL spectrometer and an inner filter effect of luminol,[21] respectively. Moreover, under electrochemical oxidation that generates the more excited form of luminol, the chemiluminescence could be significantly boosted in the presence of ROS, such as $O_2^{\bullet-}$ (Figure S4). Thus, the chemiluminescence of luminol could be triggered by different ROS or/and electrochemical oxidation. Nonetheless, it should be noted that the lifetime of $OH^{\bullet}$ (about 10^{-9}-10^{-6} s),[22] was much shorter than that of $O_2^{\bullet-}$ (about 60 s)[23] and H_2O_2 (a few days)[24] in the alkaline electrolytes, which could be utilized to deconvolute the contributions of them in ORR.

To check whether short-lived ROS could be captured by ECL, the duration of the ECL triggered by ROS was studied. As shown in Figure 2c, the ECL decay had an exponential shape (see the fitted curve using exponential function), which indicated that

the concentration of ROS near the electrode surface was exponentially decreasing in time, and practically, the concentration of ROS can be analyzed up to 10 s. Considering the consumption of ROS by ECL (Eq. 1-3) and the lifetime of ROS (e.g., ~ 1 min for $O_2^{\bullet-}$ in alkaline condition),[23] the ECL intensity after ORR was collected with an optimized time of 5 s for kinetic evaluation (Figure S7).

The last but not least critical requirement is that the introduction of ECL luminophore should not significantly influence ORR. In general, introducing excessive extraneous substances may affect the ORR kinetics.[25] Nevertheless, the polarization curves on RRDE, e.g., by Pt/C, under hydrodynamic conditions showed that such impact was weak (< 1%) in the presence of luminol up to 0.1 mM, especially in the kinetics-controlled region (Figure 2d). Such a phenomenon could be explained by the fact that an alkaline environment would weaken the adsorption strength of luminol on catalyst surfaces, thanks to an electric repulsion effect.[26] The slightly reduced limiting current of the mixed solution might be caused by the slower O_2 mass transport rate than the purely alkaline solution.[27] In this sense, by rational selecting of ECL luminophores in a proper concentration (e.g., 0.05 mM in this work), the potential interference to the ORR kinetics can be minimized.

Since all the requirements for the combined ORR and ECL reactions were satisfied, the ECL intensities by different electrocatalysts after ORR were collected using a double-potential step chronoamperometry (E_{Red}, E_{Ox}), in which E_{Red} and E_{Ox} were used to drive ORR and trigger ECL, respectively. When E_{Ox} was applied, ORR was terminated, and ECL was simultaneously activated. The duration time for ROS accumulation in ORR and the subsequent ROS consuming in ECL were optimized both to 5 s (Figure S7). Moreover, the reproducibility of these measurements was examined by repeated switching cycles (Figure S7b). Notably, ROS intermediates were not *in situ* monitored by ECL during ORR. It was because on one hand, the *in-situ* consumption of ROS by ECL may interfere with the ORR equilibrium.

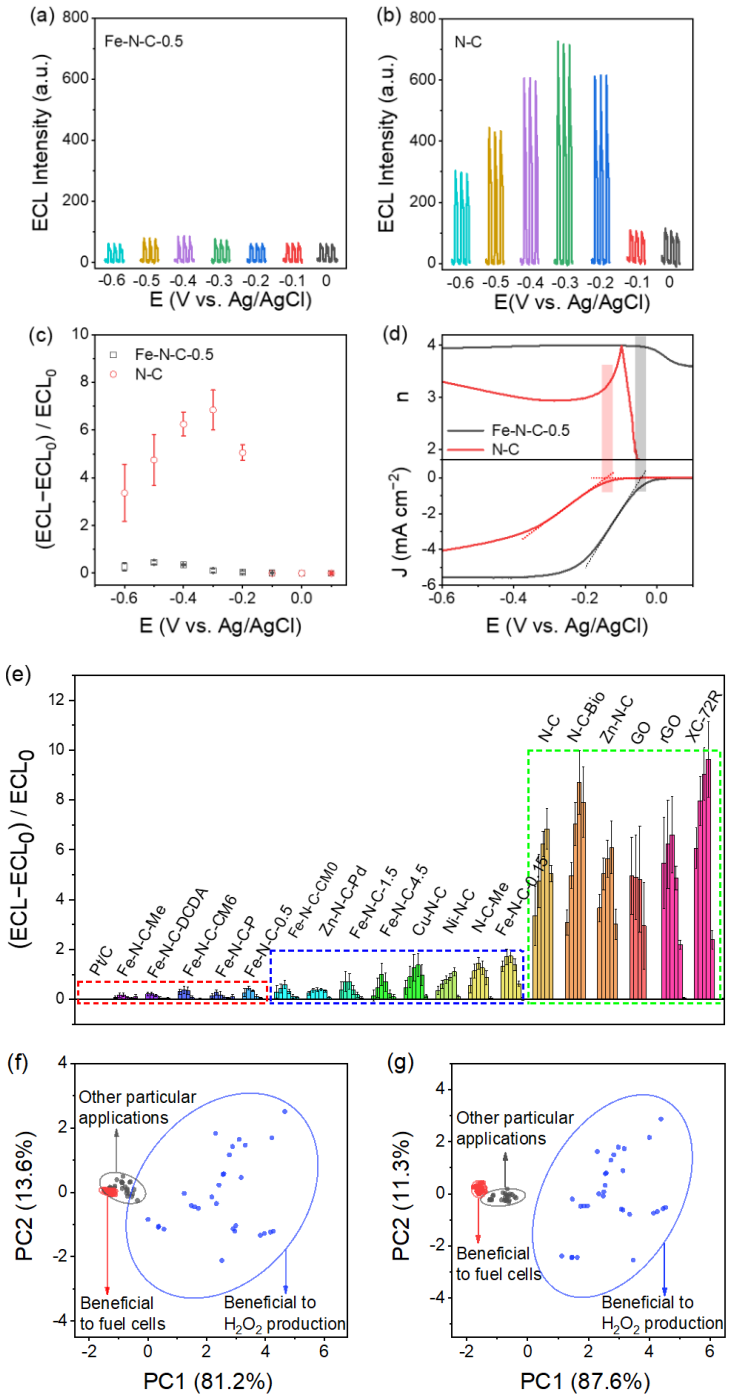

Figure 3. **Qualitative grouping ORR electrocatalysts according to electron transfer number (n) using ECL intensity.** Raw ECL signal at (a) Fe-N-C-0.5 and (b) N-C by double-potential step chronoamperometry (E_{Red}, E_{Ox}). E_{Red}: −0.6 ~ 0 V; E_{Ox}: 0.3 V. (c) Calibrated ECL intensity of Fe-N-C-0.5 and N-C at different E_{Red}. (d) Potential dependent n (top) and LSV (bottom) curves of Fe-N-C-0.5 and N-C. (e) Histogram of calibrated ECL intensity of 20 different electrocatalysts. Bar from left to right for each electrocatalyst: −0.6 ~ 0 V. The error bar represents the standard deviation. (f) PCA scatterplot from calibrated ECL intensity of different electrocatalysts. (g) PCA scatterplot from calibrated ECL intensity and reduction peak potential (E_{pc}) of different electrocatalysts. Solid cycle lines correspond to the 95% confidence interval of the spread for each cluster. Considering robust classification, five repetitive trials were independently performed for each electrocatalyst.

As proof of concept, the ECL intensity of two well-known precious group metals (PGM)-free electrocatalysts, i.e., N-C and Fe-N-C-0.5 (Figure S8 and S9), were first measured as different reduction potentials (E_{Red}). It was found that the ECL intensity of Fe-N-C-0.5 was low and almost kept constant at all measured E_{Red} (Figure 3a); while that of N-C became much higher and altered significantly at different potentials (Figure 3b). For fair comparisons, the ECL intensity at E_{Red} of 0 V and E_{Ox} of 0.3 V was set as the internal control (ECL_0) to minimize the intrinsic varieties of ECL at different electrocatalysts, and the measured ECL intensity was calibrated to the extent of ECL intensity changes ($(ECL–ECL_0)/ECL_0$). Such calibrated ECL intensity was plotted against different potentials and shown in Figure 3c. Since the ECL intensity was positively correlated with the concentration of ROS (Eq. 1-3), the marginal detected ROS depicted that the ORR of Fe-N-C-0.5 at each E_{Red} only produced a small amount of ROS. In contrast, more substantial ECL emissions from N-C were obtained, e.g., by a factor up to 100 at E_{Red} of –0.3 V (Figure 3c), manifesting the generation of abundant ROS during ORR.

As a control, the hydrodynamic linear sweep voltammetry (LSV) curves were recorded by RRDE at a rotation rate of 1600 rpm in an O_2-saturated 0.1 M KOH solution with 10 mV s^{-1} sweep rate and negative scan polarity. The associated electron transfer number (n) for the two selected electrocatalysts was shown in Figure 3d. The n value of Fe-N-C-0.5 was close to 4, particularly at the potential negative than the onset potential of –0.05 V, indicating a typical $4e^-$ pathway; while that of N-C was ca. 3, suggesting a mixed $2e^-/4e^-$ pathway. Interestingly, the change trends of calibrated ECL intensity were practically consistent with the RRDE result. Nonetheless, the RRDE method needs to manually select the reliable potential region of the as-measured ORR data, as abnormal n values were generated near the onset potential of ORR, while the ECL approach did not. In this sense, the inspection of ROS-intermediates enabled by ultrasensitive ECL showed advantages in disclosure of kinetic information of ORR with generality in the whole potential window.

Other 18 reported electrocatalysts (see Supporting Information Figure S10-25 for conventional characterizations) comprising noble metals/alloys and recent PGM-free

carbon-based catalysts were also examined by Td-ECL, showing similar results (Figure S26-45). As summarized in Figure 3e, the calibrated ECL intensity could be divided into three groups. Using the calibrated ECL intensity and n values of the well-known N-C ($3e^-$) and Fe-N-C-0.5 ($4e^-$) as the reference, the n of electrocatalysts in the same group was roughly estimated to be similar. For the other electrocatalysts, the n values were supposed to position between them. Notably, the larger difference in electron transfer number, the more distinctive Td-ECL curves. These speculations were supported by the RRDE measurements (Figure S26-45). As the Td-ECL curves could be conveniently obtained, it provided a simple yet reliable way to discriminate electrocatalysts by electron transfer numbers for H_2O_2 production or fuel cells applications.

To better associate the n value of electrocatalysts to the sophisticated ECL, the principal component analysis (PCA) that can maximize variance was further applied.[13d, 28] By reducing the dimensionality, the data set was displayed in a score plot with a coordinate system that best discriminates it. In the first attempt, the data set, including the calibrated ECL intensity obtained from various E_{Red} with five repetitive trials for each electrocatalyst, was used for the PCA processes. In the scatter graph (Figure 3f), a circle can be marked, representing an exclusive zone for a specific type of electrocatalyst, namely, beneficial to fuel cells, H_2O_2 production, or other particular applications. Nonetheless, some minor overlap of the circled zone was noted, indicating insufficient discrimination primarily because of the deficiency of uncorrelated variables. In fact, the cathodic peak potential (E_{pc}) of ORR that was simultaneously measured after the activation of electrocatalysts by cyclic voltammetry was also a typical kinetic parameter for ORR. Interestingly, further introducing E_{pc} (Table S1) into the data set for PCA, all electrocatalysts could be discriminated with the 95% confidence ellipses (Figure 3g). Therefore, based on ROS generation in ORR, the comprehensive PCA of the associated ECL intensity and E_{pc} could well discriminate electrocatalysts into different groups according to electron transfer numbers.

Beyond the qualitative classification of electrocatalysts, the quantitative determination of ORR kinetics, particularly at different potentials, is essential for the

complete evaluation of electrocatalyst performances and understanding the complicated mechanism. For this, time-dependent ECL was supposed to provide insightful information, because the ECL decay curves were closely correlated with ROS fluctuation in the diffusion layer by stoichiometric reactions; meanwhile, the time/spatial distribution of ROS is a kind of output of ORR. Thus, it suggested that the ORR kinetics can be theoretically simulated by finite element analysis (FEA) of the ECL decay curve. Figure 4a shows the ECL intensity as a function of time for different ORR electrocatalysts, which exhibited variable maxima and decay profiles, implying distinctive ORR kinetics. The ECL mechanism of luminol (LH^-, the conjugated base in alkaline solution) was outlined in Eq. 1-3 (see SI for detailed reaction mechanisms):

$$HO_2^- + OH^- - e^- \longrightarrow O_2^{\bullet-} + H_2O \quad (1)$$

$$LH^- + OH^- - e^- \longrightarrow L^{\bullet-} + H_2O \quad (2)$$

$$L^{\bullet-} + O_2^{\bullet-} \rightarrow \longrightarrow Ap^* \longrightarrow Ap + h\nu \quad (3)$$

Since the concentration of LH^- was a constant in the experiment, the amounts of photon-emitting species (Ap*) were positively correlated to that of ROS. The ECL intensity was dynamically proportional to the concentration of Ap* at any given time, depending on the relative rates of formation and consumption. The intensity of ECL was simulated by FEA by using the transient concentration of Ap* as Eq. 4:

$$I_{ECL}(t) = \phi_{ECL} \int_V [Ap^*](t)dV \quad (4)$$

where ϕ_{ECL} is the overall ECL generation and collection efficiency, t is the time, and V is the volume of Ap* solution.

For simplicity, several hypotheses and approximations were employed in establishing the rate equation. Firstly, for each electrocatalyst, the ORR reaction occurred via a mixed and competitive $2e^-$ and $4e^-$ pathway. In the $2e^-$ process, O_2 was reduced to H_2O_2 via $O_2^{\bullet-}$ intermediates, and the further reduction into H_2O via $OH^\bullet$ intermediates was ignored due to the slow reaction rate constant.[17b, 29] In the $4e^-$ process, O_2 was supposed to reduce to H_2O directly. Then, ROS production occurred only in the $2e^-$ pathway, while not in the $4e^-$ pathway. As such, a ratio of electron-transfer rate for the $4e^-$ to the $2e^-$ pathway, *m*, can describe the level of participation for each pathway.

Secondly, the reduction reaction rate of $O_2^{\bullet-}$ to H_2O_2, the rate-determining step, was assumed to be 10 times that of O_2 to $O_2^{\bullet-}$.[30] Thirdly, ROS production occurred only in the diffusion layer, and the concertation in bulk solution was set as zero.

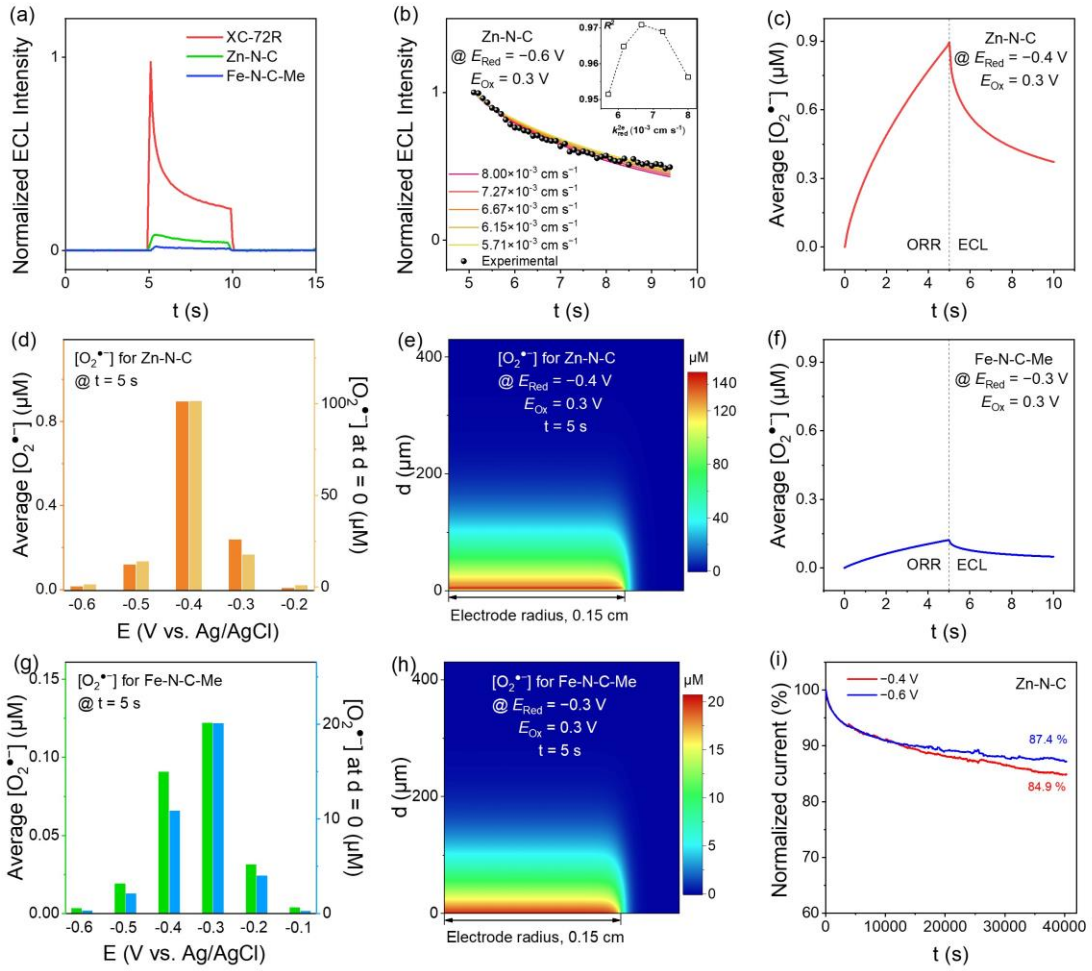

Figure 4. **Quantitative determination of ORR rate constant and distribution of ROS by ECL decay curves.** (a) ECL intensity as a function of time for XC-72R, Zn-N-C, Fe-N-C-Me. (b) Decay curves of experimental ECL data of Zn-N-C (solid black balls) and the simulated ECL curves (solid lines). Inset: the coefficient of determination (R^2) for experimental to simulated curves. (c, f) Plot of the average [$O_2^{\bullet-}$] in the diffusion layer as a function of time , (d, g) histogram of [$O_2^{\bullet-}$] in the diffusion layer under different potentials at the 5th second, and (e, h) cross-sectional view of the spatial distribution of [$O_2^{\bullet-}$] at the 5th second for (c-e) Zn-N-C (E_{Red} = –0.4 V, $E^{0,\,2e}$ = –0.38 V, and $k^{0,\,2e}$ = 6.75×10^{-4} cm s^{-1}) and (f-h) Fe-N-C-Me on GCE (E_{Red} = –0.3 V, $E^{0,\,2e}$ = –0.27 V, and $k^{0,\,2e}$ = 2.75×10^{-5} cm s^{-1}). (i) Chronoamperometric curves of Zn-N-C at –0.4 V and –0.6 V. The y-axis caption, "d", in Figure 4e and 4h indicates the distance between the electrode to the solution.

In numerical simulation, the diffusion of redox species was given by

$$\frac{\partial C_i}{\partial t} = D_i \nabla^2 c_i \qquad (5)$$

where c_i and D_i are the local concentration and diffusion coefficient of redox species i

(see SI for detailed description). The electron-transfer at the electrode surface is used as boundary condition (see SI for detailed description). To extract the apparent reaction rate constant (k_{Red}^{2e}) from the experimental ECL decay curve, a series of simulated ECL were generated through the simulation of the concertation of Ap*. For example, as shown in Figure 4b, the best fit for Zn-N-C at –0.6 V was determined from the highest coefficient of determination (R^2, see details in experimental) value, corresponding to k_{Red}^{2e} value of 6.67×10^{-3} cm s^{-1}. Notably, to eliminate the differences of potential in drive ECL of luminol by different electrocatalysts, the $k_{\text{app-LH-}}$ (the rate constant for the electro-oxidation of luminol, Eq. 2) of each electrocatalyst was corrected using the ECL_0 during the Td-ECL measurements (Figure S48, Table S6). Along this line, k_{Red}^{2e} of other typical electrocatalysts was similarly obtained (Figure S49-55), and summarized in Figure S56. Among them, XC-72R exhibited the highest k_{Red}^{2e} in this study, thus was more suitably used for H_2O_2 production. In contrast, k_{Red}^{2e} of Fe-N-C-Me was nearly two orders of magnitude lower than that of XC-72R, manifesting that Fe-N-C-Me was more inclined to a $4e^-$ reduction pathway.

Notably, despite the success in comparing the simulated k_{Red}^{2e} of different electrocatalysts, the k_{Red}^{2e} at different potential did not always follow the trend of getting larger with the increased overpotential.[29, 31] To address this deviation, instead of simply using the linear relationship between k_{Ox}^{2e} and k_{Red}^{2e} (Table S4), the Butler–Volmer (BV) formulation that quantitatively describes the relationship between the rate constant and applied potential (see more discussion in Figure S57) was further used to get more reliable k_{Red}^{2e} (Table S5), which is shown as follows (Eq. 6):

$$k_{\mathrm{Red}}^{\mathrm{BV,\,2e}} = k^{0,\,2e} e^{-\alpha \frac{F}{RT}(E_{\mathrm{Red}} - E^{0,\,2e})} \quad (6)$$

where $k_{\mathrm{Red}}^{\mathrm{BV,\,2e}}$ is the rate constant for the reduction reaction derived from the BV model, $k^{0,\,2e}$ is the standard rate constant, E_{Red} is the applied potential, $E^{0,\,2e}$ is the standard redox potential, α is the transfer coefficient, F is Faraday's constant, R is the ideal gas constant and T is the temperature.

Taking Zn-N-C of $2e^-$ pathway (Figure S58, Figure S60a) and Fe-N-C-Me of $4e^-$ pathway (Figure S59, Figure S60b) as examples, the simulated ECL intensity

approached the experimental data, resulting in ($E^{0,\,2e}$, $k^{0,\,2e}$) of (–0.38 V, 6.75×10^{-4} cm s^{-1}) and (–0.27 V, 2.75×10^{-5} cm s^{-1}), respectively. Several pioneering works had used to get k^0 values by SECM and cyclic voltammetry methods. For example, Bard *et al*. obtained k^0 of 3×10^{-3} cm s^{-1} from a simple $1e^-$ transfer of ORR in 10 M NaOH solution by SECM.[32] A voltammetry study of ORR at a methylphenyl-modified carbon electrode in 1 M KOH, $k^0 = 2.6\times10^{-4}$ cm s^{-1} was reported.[33] Compton *et al*. observed k^0 of 3×10^{-1} cm s^{-1} on a gold macroelectrode and k^0 of 2.1×10^{-1} cm s^{-1} at an electrodeposited gold nanoparticle-modified glassy carbon electrode (GCE) in 0.5 M sulfuric acid (H_2SO_4).[34] Also, they reported k^0 of 10 cm s^{-1} at a platinum nanoparticles-modified GCE in 0.5 M H_2SO_4.[30b] In addition, Hasnat *et al*. suggested a k^0 of 5.48×10^{-9} cm s^{-1} at 0.05 V vs. Ag/AgCl (sat. KCl) at gold nanoparticle-modified GCE in 0.1 M H_2SO_4.[35] It can be seen that the k^0 value has a large span in the previous works. Considering that this work examined the complicated four-electron reaction of ORR, and the electrocatalysts and electrolytes were also different from that used in previous work, the occurrence of $k^{0,\,2e}$ with different values is well documented.

On the other hand, it has been recently discussed that the free ROS radicals greatly influence the stability and durability of electrocatalysts and exchange membranes. Thus, disclosure of free radical concentration on the electrocatalyst surface (d = 0) and in the diffusion layer during the ORR is of important reference significance for optimal design of electrocatalysts for practical applications. Along this line, the variation of ROS concentration at a different time and applied potential were further simulated using the above fitted kinetic parameters. For Zn-N-C, as shown in Figure 4c, the average concentration of $O_2^{\bullet-}$ varied with time in the diffusion layer, and the fluctuation of $O_2^{\bullet-}$ concentration was observed, corresponding to the overall effect of the production in ORR process and the consumption in ECL measurements. In addition, the concentration of $O_2^{\bullet-}$ at the electrocatalyst surface or in the diffusion layer, firstly became higher and later decreased with the increase of overpotentials (Figure 4d). Conversely, simulated concentration of H_2O_2 kept increasing with the increase of overpotentials (Figure S61). The side-view of the simulated concentration profile of $O_2^{\bullet-}$ in Figure 4e clearly demonstrating the concentration distribution of ROS in the diffusion layer. Interestingly,

the $O_2^{\bullet-}$ concentration for Fe-N-C-Me at different time and potentials was much lower than that for Zn-N-C, but the trend was similar (Figure 4f, g, h). The complete time and spatial distribution of H_2O_2 and $O_2^{\bullet-}$ at Zn-N-C and Fe-N-C-Me are shown in Movie S1-4. Notably, $OH^{\bullet}$ was frequently discussed in the destabilization of electrocatalysts in acidic media, but the role of $O_2^{\bullet-}$ has been rarely studied, thus we could not rule out the possibility of a similar destabilizing effect by $O_2^{\bullet-}$ that was dominantly produced in alkaline media.[12a] In this regard, it was assumed that the selection of a larger overpotential would be beneficial to electrocatalysts of $2e^-$ reduction pathway for H_2O_2 production, because of simultaneous getting high yield of H_2O_2 and low concentration of attackable $O_2^{\bullet-}$. In contrast, the choice of a smaller overpotential would be preferred to electrocatalysts of $4e^-$ reduction pathway for fuel cells, owing to the simultaneously lower concentration of attackable $O_2^{\bullet-}$ and higher output voltage.

Such time/spatial distribution information of ROS was critical in guiding the specific application of ORR electrocatalysts to acquire both maximized electrochemical performance and stability. Nonetheless, it should be noted that MEA[6d], RDE/RRDE[6d], SECM[11d], and some advanced surface-sensitive spectroscopic methods (e.g., SERS[10b]) generally cannot supply such information. To validate the above measured concentration information of ROS, the electrocatalysts stability test was performed at different reduction potentials. As shown in Figure 4i, the chronoamperometric curves showed the reduction current of Zn-N-C decreased to 84.9% and 87.4% of their initial current density after 40,000 s at −0.4 V and −0.6 V, respectively. It indicated that for H_2O_2 production herein a larger overpotential was favor of maintaining the stability, which supported the above measurement of less attackable ROS (Figure 4d).

Conclusion

In summary, we devised a simple yet powerful intermediate-oriented strategy for the kinetic evaluation of ORR electrocatalyst by time-dependent ECL. It utilized ROS intermediates during the ORR process to establish the reaction rate equation, which endowed a strong correlation between trace ROS and ECL thanks to multiple ultrasensitive stoichiometric reactions. It was found that the closer to the $2e^-$ or $4e^-$

reduction, the more distinctive Td-ECL curve, thus ORR electrocatalysts could be reliably discriminated for H_2O_2 production or fuel cells applications. Moreover, beyond ORR selectivity and rate constant, the potential-dependent time and spatial distribution of ROS in the diffusion layer was successfully derived for the first time from the Td-ECL decay curves by finite element analysis. Such uncovered exclusive information was validated preliminarily by the stability evaluation of electrocatalyst, and would guide fuel cells and H_2O_2 production with maximized activity and durability. Besides, only commonly-used potentiostat, glassy carbon electrodes, and a photomultiplier were needed for synchronous ORR operation and Td-ECL collection, which simplified the instrumentation and broadened the applicable scope. This work would provide a facile way to understand more detailed ORR kinetics and pave the way for the rational development of ORR electrocatalysts in practical applications.

In this work, the rate equation and simulation make some simplifying assumptions, and it is undoubtedly important to be aware of the validity of these assumptions as we refine this approach in the future. For instance, the detailed adsorption/desorption of O_2, ROS, and luminol on the electrocatalysts was not strictly considered. The adsorption/desorption of reactants, intermidiates and products generally occur, and are widely explored along with electron transfers by spectroscopic techniques and density functional theory (DFT) calculation to understand the possible rate-determining step (RDS).[36] In practice, either the first or the last electron transfer step was often considered to be RDS for ORR of PGM-free electrocatalysts in alkaline media,[37] while the present work only discussed the first electron transfer step as the RDS. Although ORR kinetics of several typical PGM-free electrocatalysts was obtained reasonably by simulation in this study, more careful consideration of adsorption/desorption processes and the last electron transfer step as the potential RDS is needed in the further work, particularly for new electrocatalysts. In addition, luminol, a broad-spectrum ECL emitter for all types of ROS, was used in this study. On the other hand, ECL probe molecules with selectivity will be beneficial for capturing the specific type of ROS for ORR and offering more complete ORR mechanisms. Work focused on these exciting subjects is ongoing.

References

1. (a) Ahn, C.-Y.; Park, J. E.; Kim, S.; Kim, O.-H.; Hwang, W.; Her, M.; Kang, S. Y.; Park, S.; Kwon, O. J.; Park, H. S.; Cho, Y.-H.; Sung, Y.-E., Differences in the Electrochemical Performance of Pt-Based Catalysts Used for Polymer Electrolyte Membrane Fuel Cells in Liquid Half- and Full-Cells. *Chem. Rev.* **2021,** *121*, 15075-15140. **(b)** He, Y.; Liu, S.; Priest, C.; Shi, Q.; Wu, G., Atomically dispersed metal–nitrogen–carbon catalysts for fuel cells: advances in catalyst design, electrode performance, and durability improvement. *Chem. Soc. Rev.* **2020,** *49*, 3484-3524. **(c)** Debe, M. K., Electrocatalyst approaches and challenges for automotive fuel cells. *Nature* **2012,** *486*, 43-51. **(d)** Kodama, K.; Nagai, T.; Kuwaki, A.; Jinnouchi, R.; Morimoto, Y., Challenges in applying highly active Pt-based nanostructured catalysts for oxygen reduction reactions to fuel cell vehicles. *Nat. Nanotechnol.* **2021,** *16*, 140-147. **(e)** Yu, P.; Wang, L.; Sun, F.; Xie, Y.; Liu, X.; Ma, J.; Wang, X.; Tian, C.; Li, J.; Fu, H., Co Nanoislands Rooted on Co–N–C Nanosheets as Efficient Oxygen Electrocatalyst for Zn–Air Batteries. *Adv. Mater.* **2019**. **(f)** Jiang, Y.; Deng, Y.-P.; Liang, R.; Fu, J.; Gao, R.; Luo, D.; Bai, Z.; Hu, Y.; Yu, A.; Chen, Z., d-Orbital steered active sites through ligand editing on heterometal imidazole frameworks for rechargeable zinc-air battery. *Nat. Commun.* **2020,** *11*.

2. Nørskov, J. K.; Rossmeisl, J.; Logadottir, A.; Lindqvist, L.; Kitchin, J. R.; Bligaard, T.; Jónsson, H., Origin of the Overpotential for Oxygen Reduction at a Fuel-Cell Cathode. *J. Phys. Chem. B* **2004,** *108*, 17886-17892.

3. (a) Liu, Z.; Zhao, Z.; Peng, B.; Duan, X.; Huang, Y., Beyond Extended Surfaces: Understanding the Oxygen Reduction Reaction on Nanocatalysts. *J. Am. Chem. Soc.* **2020,** *142*, 17812-17827. **(b)** Jiao, L.; Li, J.; Richard, L. L.; Sun, Q.; Stracensky, T.; Liu, E.; Sougrati, M. T.; Zhao, Z.; Yang, F.; Zhong, S.; Xu, H.; Mukerjee, S.; Huang, Y.; Cullen, D. A.; Park, J. H.; Ferrandon, M.; Myers, D. J.; Jaouen, F.; Jia, Q., Chemical vapour deposition of Fe–N–C oxygen reduction catalysts with full utilization of dense Fe–N4 sites. *Nat. Mater.* **2021,** *20*, 1385-1391. **(c)** Seh, Z. W.; Kibsgaard, J.; Dickens, C. F.; Chorkendorff, I.; Nørskov, J. K.; Jaramillo, T. F., Combining theory and experiment in electrocatalysis: Insights into materials design. *Science* **2017,** *355*.

4. Zaman, S.; Huang, L.; Douka, A. I.; Yang, H.; You, B.; Xia, B. Y., Oxygen Reduction Electrocatalysts toward Practical Fuel Cells: Progress and Perspectives. *Angew. Chem. Int. Ed.* **2021,** *60*, 17832-17852.

5. Martens, S.; Asen, L.; Ercolano, G.; Dionigi, F.; Zalitis, C.; Hawkins, A.; Martinez Bonastre, A.; Seidl, L.; Knoll, A. C.; Sharman, J.; Strasser, P.; Jones, D.; Schneider, O., A comparison of rotating disc electrode, floating electrode technique and membrane electrode assembly measurements for catalyst testing. *J. Power Sources* **2018,** *392*, 274-284.

6. (a) Zhou, R.; Zheng, Y.; Jaroniec, M.; Qiao, S.-Z., Determination of the Electron Transfer Number for the Oxygen Reduction Reaction: From Theory to Experiment. *ACS Catal.* **2016,** *6*, 4720-4728. **(b)** Dong, K.; Liang, J.; Wang, Y.; Xu, Z.; Liu, Q.; Luo, Y.; Li, T.; Li, L.; Shi, X.; Asiri, A. M.; Li, Q.; Ma, D.; Sun, X., Honeycomb Carbon Nanofibers: A Superhydrophilic O_2-Entrapping Electrocatalyst Enables Ultrahigh Mass Activity for the Two-Electron Oxygen Reduction Reaction. *Angew. Chem. Int. Ed.* **2021,** *60*, 10583-10587. **(c)** Yang, Z.; Yang, H.; Shang, L.; Zhang, T., Ordered PtFeIr Intermetallic Nanowires Prepared through a Silica-Protection Strategy for the Oxygen Reduction Reaction. *Angew. Chem. Int. Ed.* **2021,** *61*. **(d)** Fan, J.; Chen, M.; Zhao, Z.; Zhang, Z.; Ye, S.; Xu, S.; Wang, H.; Li, H., Bridging the gap between highly active oxygen reduction reaction catalysts and effective catalyst layers for proton exchange membrane fuel cells. *Nat. Energy* **2021,** *6*, 475-486.

7. Yang, Y.; Peltier, C. R.; Zeng, R.; Schimmenti, R.; Li, Q.; Huang, X.; Yan, Z.; Potsi, G.; Selhorst, R.; Lu, X.; Xu, W.; Tader, M.; Soudackov, A. V.; Zhang, H.; Krumov, M.; Murray, E.; Xu, P.; Hitt, J.; Xu, L.;

Ko, H.-Y.; Ernst, B. G.; Bundschu, C.; Luo, A.; Markovich, D.; Hu, M.; He, C.; Wang, H.; Fang, J.; DiStasio, R. A.; Kourkoutis, L. F.; Singer, A.; Noonan, K. J. T.; Xiao, L.; Zhuang, L.; Pivovar, B. S.; Zelenay, P.; Herrero, E.; Feliu, J. M.; Suntivich, J.; Giannelis, E. P.; Hammes-Schiffer, S.; Arias, T.; Mavrikakis, M.; Mallouk, T. E.; Brock, J. D.; Muller, D. A.; DiSalvo, F. J.; Coates, G. W.; Abruña, H. D., Electrocatalysis in Alkaline Media and Alkaline Membrane-Based Energy Technologies. *Chem. Rev.* **2022,** *122*, 6117-6321.

8. Mustain, W. E.; Chatenet, M.; Page, M.; Kim, Y. S., Durability challenges of anion exchange membrane fuel cells. *Energy Environ. Sci.* **2020,** *13*, 2805-2838.

9. (a) Shao, M.-h.; Liu, P.; Adzic, R. R., Superoxide Anion is the Intermediate in the Oxygen Reduction Reaction on Platinum Electrodes. *J. Am. Chem. Soc.* **2006,** *128*, 7408-7409. **(b)** Ohta, N.; Nomura, K.; Yagi, I., Adsorption and Electroreduction of Oxygen on Gold in Acidic Media: In Situ Spectroscopic Identification of Adsorbed Molecular Oxygen and Hydrogen Superoxide. *J. Phys. Chem. C* **2012,** *116*, 14390-14400.

10. (a) Johnson, L.; Li, C.; Liu, Z.; Chen, Y.; Freunberger, S. A.; Ashok, P. C.; Praveen, B. B.; Dholakia, K.; Tarascon, J.-M.; Bruce, P. G., The role of LiO2 solubility in O2 reduction in aprotic solvents and its consequences for Li–O2 batteries. *Nat. Chem.* **2014,** *6*, 1091-1099. **(b)** Dong, J.-C.; Zhang, X.-G.; Briega-Martos, V.; Jin, X.; Yang, J.; Chen, S.; Yang, Z.-L.; Wu, D.-Y.; Feliu, J. M.; Williams, C. T.; Tian, Z.-Q.; Li, J.-F., In situ Raman spectroscopic evidence for oxygen reduction reaction intermediates at platinum single-crystal surfaces. *Nat. Energy* **2018,** *4*, 60-67.

11. (a) Bard, A. J.; Fan, F.-R. F.; Pierce, D. T.; Unwin, P. R.; Wipf, D. O.; Zhou, F., Chemical Imaging of Surfaces with the Scanning Electrochemical Microscope. *Science* **1991,** *254*, 68-74. **(b)** Amemiya, S.; Bard, A. J.; Fan, F.-R. F.; Mirkin, M. V.; Unwin, P. R., Scanning Electrochemical Microscopy. *Annu. Rev. Anal. Chem.* **2008,** *1*, 95-131. **(c)** Preet, A.; Lin, T.-E., A Review: Scanning Electrochemical Microscopy (SECM) for Visualizing the Real-Time Local Catalytic Activity. *Catalysts* **2021,** *11*. **(d)** Zhou, M.; Yu, Y.; Hu, K.; Mirkin, M. V., Nanoelectrochemical Approach To Detecting Short-Lived Intermediates of Electrocatalytic Oxygen Reduction. *J. Am. Chem. Soc.* **2015,** *137*, 6517-6523.

12. (a) Wierzbicki, S.; Douglin, J. C.; Kostuch, A.; Dekel, D. R.; Kruczała, K., Are Radicals Formed During Anion-Exchange Membrane Fuel Cell Operation? *J. Phys. Chem. Lett.* **2020,** *11*, 7630-7636. **(b)** Zhang, Y.; Parrondo, J.; Sankarasubramanian, S.; Ramani, V., Detection of Reactive Oxygen Species in Anion Exchange Membrane Fuel Cells using In Situ Fluorescence Spectroscopy. *ChemSusChem* **2017,** *10*, 3056-3062. **(c)** Xu, W.; Kong, J. S.; Yeh, Y.-T. E.; Chen, P., Single-molecule nanocatalysis reveals heterogeneous reaction pathways and catalytic dynamics. *Nat. Mater.* **2008,** *7*, 992-996. **(d)** Xiao, Y.; Hong, J.; Wang, X.; Chen, T.; Hyeon, T.; Xu, W., Revealing Kinetics of Two-Electron Oxygen Reduction Reaction at Single-Molecule Level. *J. Am. Chem. Soc.* **2020,** *142*, 13201-13209.

13. (a) Chen, M.-M.; Xu, C.-H.; Zhao, W.; Chen, H.-Y.; Xu, J.-J., Super-Resolution Electrogenerated Chemiluminescence Microscopy for Single-Nanocatalyst Imaging. *J. Am. Chem. Soc.* **2021,** *143*, 18511-18518. **(b)** Maar, R. R.; Zhang, R.; Stephens, D. G.; Ding, Z.; Gilroy, J. B., Near-Infrared Photoluminescence and Electrochemiluminescence from a Remarkably Simple Boron Difluoride Formazanate Dye. *Angew. Chem. Int. Ed.* **2019,** *58*, 1052-1056. **(c)** Ma, X.; Gao, W.; Du, F.; Yuan, F.; Yu, J.; Guan, Y.; Sojic, N.; Xu, G., Rational Design of Electrochemiluminescent Devices. *Acc. Chem. Res.* **2021,** *54*, 2936-2945. **(d)** Dong, J.; Lu, Y.; Xu, Y.; Chen, F.; Yang, J.; Chen, Y.; Feng, J., Direct imaging of single-molecule electrochemical reactions in solution. *Nature* **2021,** *596*, 244-249. **(e)** Lv, Y.; Chen, S.; Shen, Y.; Ji, J.; Zhou, Q.; Liu, S.; Zhang, Y., Competitive Multiple-Mechanism-Driven Electrochemiluminescent Detection of 8-Hydroxy-2′-deoxyguanosine. *J. Am. Chem. Soc.* **2018,** *140*,

2801-2804. **(f)** Gu, W.; Wang, H.; Jiao, L.; Wu, Y.; Chen, Y.; Hu, L.; Gong, J.; Du, D.; Zhu, C., Single-Atom Iron Boosts Electrochemiluminescence. *Angew. Chem. Int. Ed.* **2020,** *59*, 3534-3538. **(g)** Haapakka, K. E.; Kankare, J. J., The mechanism of the electrogenerated chemiluminescence of luminol in aqueous alkaline solution. *Anal. Chim. Acta* **1982,** *138*, 263-275. **(h)** Zanut, A.; Fiorani, A.; Canola, S.; Saito, T.; Ziebart, N.; Rapino, S.; Rebeccani, S.; Barbon, A.; Irie, T.; Josel, H.-P.; Negri, F.; Marcaccio, M.; Windfuhr, M.; Imai, K.; Valenti, G.; Paolucci, F., Insights into the mechanism of coreactant electrochemiluminescence facilitating enhanced bioanalytical performance. *Nat. Commun.* **2020,** *11*.

14. (a) Li, H.; Daniel, J.; Verlhac, J.-B.; Blanchard-Desce, M.; Sojic, N., Bright Electrogenerated Chemiluminescence of a Bis-Donor Quadrupolar Spirofluorene Dye and Its Nanoparticles. *Chem. Eur. J.* **2016,** *22*, 12702-12714. **(b)** Miao, W., Electrogenerated Chemiluminescence and Its Biorelated Applications. *Chem. Rev.* **2008,** *108*, 2506-2553. **(c)** Mahé, É.; Bornoz, P.; Briot, E.; Chevalet, J.; Comninellis, C.; Devilliers, D., A selective chemiluminescence detection method for reactive oxygen species involved in oxygen reduction reaction on electrocatalytic materials. *Electrochim. Acta* **2013,** *102*, 259-273. **(d)** Xia, H.; Zheng, X.; Li, J.; Wang, L.; Xue, Y.; Peng, C.; Han, Y.; Wang, Y.; Guo, S.; Wang, J.; Wang, E., Identifying Luminol Electrochemiluminescence at the Cathode via Single-Atom Catalysts Tuned Oxygen Reduction Reaction. *J. Am. Chem. Soc.* **2022,** *144*, 7741-7749.

15. Zhao, W.; Chen, H.-Y.; Xu, J.-J., Electrogenerated chemiluminescence detection of single entities. *Chem. Sci.* **2021,** *12*, 5720-5736.

16. (a) Kuwana, T., Electro-oxidation followed by light emmission. *J. Electroanal. Chem. (1959)* **1963,** *6*, 164-167. **(b)** Merényi, G.; Lind, J.; Eriksen, T. E., Luminol chemiluminescence: Chemistry, excitation, emitter. *J. Biolumin. Chemilumin.* **1990,** *5*, 53-56.

17. (a) Hsueh, K. L.; Chin, D. T.; Srinivasan, S., Electrode kinetics of oxygen reduction. *J. Electroanal. Chem.* **1983,** *153*, 79-95. **(b)** Wu, F.; Pan, C.; He, C.-T.; Han, Y.; Ma, W.; Wei, H.; Ji, W.; Chen, W.; Mao, J.; Yu, P.; Wang, D.; Mao, L.; Li, Y., Single-Atom Co–N4 Electrocatalyst Enabling Four-Electron Oxygen Reduction with Enhanced Hydrogen Peroxide Tolerance for Selective Sensing. *J. Am. Chem. Soc.* **2020,** *142*, 16861-16867.

18. Wang, J.; Wang, K.; Wang, F.-B.; Xia, X.-H., Bioinspired copper catalyst effective for both reduction and evolution of oxygen. *Nat. Commun.* **2014,** *5*.

19. (a) Bardouki, H.; da Rosa, M. B.; Mihalopoulos, N.; Palm, W. U.; Zetzsch, C., Kinetics and mechanism of the oxidation of dimethylsulfoxide (DMSO) and methanesulfinate (MSI−) by OH radicals in aqueous medium. *Atmos. Environ.* **2002,** *36*, 4627-4634. **(b)** Schiller, J.; Arnhold, J.; Schwinn, J.; Sprinz, H.; Brede, O.; Arnold, K., Differences in the reactivity of phthalic hydrazide and luminol with hydroxyl radicals. *Free Radic. Res.* **2009,** *30*, 45-57.

20. (a) Bandara, J.; Kiwi, J., Fast kinetic spectroscopy, decoloration and production of H2O2 induced by visible light in oxygenated solutions of the azo dye Orange II. *New J. Chem.* **1999,** *23*, 717-724. **(b)** Koizumi, Y.; Nosaka, Y., Kinetics Simulation of Luminol Chemiluminescence Based on Quantitative Analysis of Photons Generated in Electrochemical Oxidation. *J. Phys. Chem. A* **2013,** *117*, 7705-7711.

21. Sartin, M. M.; Camerel, F.; Ziessel, R.; Bard, A. J., Electrogenerated Chemiluminescence of B8amide: A BODIPY-Based Molecule with Asymmetric ECL Transients. *J. Phys. Chem. C* **2008,** *112*, 10833-10841.

22. (a) Chen, L.-N.; Yu, W.-S.; Wang, T.; Yang, X.-D.; Yang, H.-J.; Chen, Z.-X.; Wang, T.; Tian, N.; Zhou, Z.-Y.; Sun, S.-G., Fluorescence detection of hydroxyl radical generated from oxygen reduction on Fe/N/C catalyst. *Sci. China Chem.* **2019,** *63*, 198-202. **(b)** Tampieri, F.; Ginebra, M.-P.; Canal, C., Quantification of Plasma-Produced Hydroxyl Radicals in Solution and their Dependence on the pH. *Anal. Chem.* **2021,**

93, 3666-3670.

23. Zang, L. Y.; Misra, H. P., EPR kinetic studies of superoxide radicals generated during the autoxidation of 1-methyl-4-phenyl-2,3-dihydropyridinium, a bioactivated intermediate of parkinsonian-inducing neurotoxin 1-methyl-4-phenyl-1,2,3,6-tetrahydropyridine. *J. Biol. Chem.* **1992,** *267*, 23601-23608.

24. Jung, Y. S.; Lim, W. T.; Park, J. Y.; Kim, Y. H., Effect of pH on Fenton and Fenton-like oxidation. *Environ. Technol.* **2009,** *30*, 183-190.

25. (a) Qu, L.; Liu, Y.; Baek, J.-B.; Dai, L., Nitrogen-Doped Graphene as Efficient Metal-Free Electrocatalyst for Oxygen Reduction in Fuel Cells. *ACS Nano* **2010,** *4*, 1321-1326. **(b)** He, D.; Zhong, L.; Gan, S.; Xie, J.; Wang, W.; Liu, Z.; Guo, W.; Yang, X.; Niu, L., Hydrogen peroxide electrosynthesis via regulating the oxygen reduction reaction pathway on Pt noble metal with ion poisoning. *Electrochim. Acta* **2021,** *371*.

26. (a) Zhu, S.; Hu, X.; Shao, M., Impacts of anions on the oxygen reduction reaction kinetics on platinum and palladium surfaces in alkaline solutions. *Phys. Chem. Chem. Phys.* **2017,** *19*, 7631-7641. **(b)** Holst-Olesen, K.; Reda, M.; Hansen, H. A.; Vegge, T.; Arenz, M., Enhanced Oxygen Reduction Activity by Selective Anion Adsorption on Non-Precious-Metal Catalysts. *ACS Catal.* **2018,** *8*, 7104-7112.

27. Omura, J.; Yano, H.; Watanabe, M.; Uchida, H., Electrochemical Quartz Crystal Microbalance Analysis of the Oxygen Reduction Reaction on Pt-Based Electrodes. Part 1: Effect of Adsorbed Anions on the Oxygen Reduction Activities of Pt in HF, HClO4, and H2SO4 Solutions. *Langmuir* **2011,** *27*, 6464-6470.

28. Stewart, S.; Ivy, M. A.; Anslyn, E. V., The use of principal component analysis and discriminant analysis in differential sensing routines. *Chem. Soc. Rev.* **2014,** *43*, 70-84.

29. Muthukrishnan, A.; Nabae, Y.; Okajima, T.; Ohsaka, T., Kinetic Approach to Investigate the Mechanistic Pathways of Oxygen Reduction Reaction on Fe-Containing N-Doped Carbon Catalysts. *ACS Catal.* **2015,** *5*, 5194-5202.

30. (a) Gómez-Marín, A. M.; Feliu, J. M.; Ticianelli, E., Oxygen Reduction on Platinum Surfaces in Acid Media: Experimental Evidence of a CECE/DISP Initial Reaction Path. *ACS Catalysis* **2019,** *9*, 2238-2251. **(b)** Gara, M.; Laborda, E.; Holdway, P.; Crossley, A.; Jones, C. J. V.; Compton, R. G., Oxygen reduction at sparse arrays of platinum nanoparticles in aqueous acid: hydrogen peroxide as a liberated two electron intermediate. *Phys. Chem. Chem. Phys.* **2013,** *15*.

31. Kato, M.; Fujibayashi, N.; Abe, D.; Matsubara, N.; Yasuda, S.; Yagi, I., Impact of Heterometallic Cooperativity of Iron and Copper Active Sites on Electrocatalytic Oxygen Reduction Kinetics. *ACS Catal.* **2021,** *11*, 2356-2365.

32. Zhang, C.; Fan, F.-R. F.; Bard, A. J., Electrochemistry of Oxygen in Concentrated NaOH Solutions: Solubility, Diffusion Coefficients, and Superoxide Formation. *J. Am. Chem. Soc.* **2008,** *131*, 177-181.

33. Yang, H.-H.; McCreery, R. L., Elucidation of the Mechanism of Dioxygen Reduction on Metal-Free Carbon Electrodes. *J. Electrochem. Soc.* **2000,** *147*.

34. Wang, Y.; Laborda, E.; Ward, K. R.; Tschulik, K.; Compton, R. G., A kinetic study of oxygen reduction reaction and characterization on electrodeposited gold nanoparticles of diameter between 17 nm and 40 nm in 0.5 M sulfuric acid. *Nanoscale* **2013,** *5*.

35. Islam, M. T.; Hasan, M. M.; Shabik, M. F.; Islam, F.; Nagao, Y.; Hasnat, M. A., Electroless deposition of gold nanoparticles on a glassy carbon surface to attain methylene blue degradation via oxygen reduction reactions. *Electrochim. Acta* **2020,** *360*.

36. Kulkarni, A.; Siahrostami, S.; Patel, A.; Nørskov, J. K., Understanding Catalytic Activity Trends in

the Oxygen Reduction Reaction. *Chem. Rev.* **2018,** *118*, 2302-2312.
37. (a) Chen, Y.; Ji, S.; Wang, Y.; Dong, J.; Chen, W.; Li, Z.; Shen, R.; Zheng, L.; Zhuang, Z.; Wang, D.; Li, Y., Isolated Single Iron Atoms Anchored on N-Doped Porous Carbon as an Efficient Electrocatalyst for the Oxygen Reduction Reaction. *Angew. Chem. Int. Ed.* **2017,** *56*, 6937-6941. **(b)** Gao, L.; Xiao, M.; Jin, Z.; Liu, C.; Zhu, J.; Ge, J.; Xing, W., Correlating Fe source with Fe-N-C active site construction: Guidance for rational design of high-performance ORR catalyst. *J. Energy Chem.* **2018,** *27*, 1668-1673. **(c)** Lu, Y.-R.; Chen, H.-C.; Liu, K.; Liu, M.; Chan, T.-S.; Hung, S.-F., Turn the Trash into Treasure: Egg-White-Derived Single-Atom Electrocatalysts Boost Oxygen Reduction Reaction. *ACS Sustain. Chem. Eng.* **2022,** *10*, 6736-6742.